Structure defined 2D Mo₂C/2Dg-C₃N₄ Van der Waals heterojunction: Oriented charge flow in-plane and separation within the interface to collectively promote photocatalytic degradation of pharmaceutical and personal care products

Yin Zhou [a,b], Chen Zhang [a,b,*], Danlian Huang [a,b,*], Wenjun Wang [a,b], Yunbo Zhai [a,b,*], Qinghua Liang [a,b], Yang Yang [a,b], Suhong Tian [a,b], Hanzhuo Luo [a,b], Deyu Qin [a,b]

[a] College of Environmental Science and Engineering, Hunan University, Changsha 410082, PR China
[b] Key Laboratory of Environmental Biology and Pollution Control, Hunan University, Ministry of Education, Changsha 410082, PR China

ARTICLE INFO

ABSTRACT

Pharmaceuticals and personal care products (PPCPs) are a large class of emerging contaminants. Here, we develop a 2D/2D Mo₂C/g-C₃N₄ Van der Waals (VDW) heterojunction photocatalyst for typical PPCPs degradation. The 2D Mo₂C shows unique electronic transport properties and allows the integration with other 2D materials for fabricating intriguing 2D interface. The Mo₂C strongly coordinates with g-C₃N₄ to endow the ordered in-plane electron migration in g-C₃N₄ nanosheets and the VDW forces induce the electrons transfer within interlayers, building an internal electric field and stimulating the photogenerated charge kinetics. In addition, Mo₂C can ameliorate the light absorption capacity and trap electrons to elongate the lifetimes of charge carriers. This synergy between VDW heterojunction and 2D structure engineering contributes to the superior photocatalytic activity for tetracycline degradation. Advanced characterizations, charge density based on density function theory calculations and the absence of charge transfer between layers confirm the VDW interactions between the individual components. This work provides a highly efficient and green strategy for typical PPCPs removal, and sheds lights on the construction of 2D/2D VDW heterojunction photocatalysts.

1. Introduction

Pharmaceuticals and personal care products (PPCPs) are a large class of emerging contaminants, such as various antibiotics, anti-inflammatory drugs, hormones, and antimicrobial agents [1]. With the mass production and application of PPCPs, the potential threats to human health and whole ecosystem caused by the outpouring PPCPs is gradually increasing [2]. Among them, the typical PPCPs are antibiotic contamination. China is the world's largest antibiotic producer and consumer. A total of 110 antibiotics have been detected, of which 28 priority antibiotics are ubiquitous in almost all environment compartments in China [3]. Tetracycline (TC) is defined to be one of the dominant antibiotics and has drawn tremendous attention [4]. The threat of these chemicals to human health forces people to formulate effective strategies to eliminate the impact of these compounds [5]. Recently, photocatalytic technology is regarded as a promising strategy

for the treatment of antibiotic wastewater and is gaining more attention [6]. The use of solar radiation means the minimization of energy consumption and therefore the least impact on the environment [7,8]. The reactive oxygen species generated during the photocatalytic process could decompose the pollutants effectively [9]. After years of development, some progress has been made in the photocatalysis of antibiotic wastewater. For examples, Zhu et al. investigated the kinetics and mechanism of photocatalytic degradation TC by perylene diimide supramolecular (PDI) organic photocatalyst [10]. The PDI organic catalyst showed excellent photocatalytic performance and stability to TC degradation. Sun et al. synthesized ZnSnO₃ hollow cube photocatalyst for efficient treatment of antibiotic wastewater [11]. The hollow structure provides a platform for the direct interaction between pollutants and photocatalysts, facilitating the adsorption and degradation kinetics. The photocatalytic technology for high-efficiency degradation of antibiotics in the water treatment field is worthy to be studied.

---

* Corresponding authors at: College of Environmental Science and Engineering, Hunan University, Changsha 410082, PR China.
E-mail addresses: zhangchen@hnu.edu.cn (C. Zhang), huangdanlian@hnu.edu.cn (D. Huang), ybzhai@hnu.edu.cn (Y. Zhai).

Among the numerous explored photocatalysts, graphitic carbon nitride (g-C$_3$N$_4$) has received increasing attention due to its favorable band gap, excellent chemical and thermal stability, environmental benignity, and earth abundance [12]. g-C$_3$N$_4$ based photocatalysts have been widely applied in alcohol oxidation, hydrogen evolution, pollutant degradation, hydrogen peroxide production and other advanced photo-oxidation reactions [13,14]. However, the catalytic performance of g-C$_3$N$_4$ is largely limited by the low separation efficiency and fast recombination of charge carriers [15]. Hence over the years, extensive strategies have been adopted to conquer this limitation. In particular, a robust strategy is to construct heterostructure via assembling different components by physical and chemical interactions, such as covalent bonding, VDW force, ionic bonding and Coulomb force [16].

Among them, the emerging 2D/2D VDW heterojunction opens a new avenue for the development of photocatalysis both in scientific research and technological application. VDW heterojunctions are assembled through VDW interactions, which allows researchers to restack 2D materials into arbitrary stacking junctions without the consideration of the lattice matching between layers and atomic interdiffusion that exist in the growth of conventional covalently bonded semiconductor based heterostructures, thus possessing huge potential and versatility for developing new 2D/2D materials [17]. Comparing with isolated materials, the 2D/2D VDW heterojunction can achieve exceptional electrical, optical, and photocatalytic properties. For example, the 2D/2D ZnIn$_2$S$_4$/g-C$_3$N$_4$ VDW heterojunction with S vacancies photocatalyst was engineered for capturing more electrons [18]. The construction of g-C$_3$N$_4$/C-doped BN VDW heterojunction has revealed remarkable hydrogen yield from water [19]. The VDW force serves as the intermolecular, furnishing driving force for electrons transfer. The strong electronic coupling between layers contributes to the improved catalytic activity. In addition, the unique "face-to-face" contact is conducive to the formation of large interface area and strong interactions. Decreasing the thickness greatly minimizes the migration distance of photo-induced electrons and increases the number of active sites, leading to the enhancement of photocatalytic performance. Furthermore, plenty of high-speed charge transfer channels emerge at the 2D/2D VDW hetero-interface, which is favorable for the convenient migration of charge carriers [20]. Inspired by this, the fabrication of g-C$_3$N$_4$ based 2D/2D VDW heterojunction is an efficient and alternative way to improve the photocatalytic efficiency and the metal-free 2D g-C$_3$N$_4$ also provides a wide variety of combinations with other 2D materials.

Mo$_2$C, a new member of MXenes, has attracted tremendous attention due to its intriguing properties such as high conductivity, excellent stability, and excellent photoelectric properties [21,22]. Particularly, Mo$_2$C has been widely studied and demonstrated promise in photoelectric catalysis [23], thermoelectricity [24] and energy storage [25]. The 2D Mo$_2$C shows unique grain boundaries and electronic transport properties and allows the integration with other 2D materials for intriguing physics at the 2D interfaces [21]. Most importantly, Mo$_2$C can enhance the visible light absorption of g-C$_3$N$_4$ and trap electrons to restrict the recombination of charge carriers [26,27]. Based on these, constructing 2D/2D Mo$_2$C/g-C$_3$N$_4$ VDW heterojunction would be beneficial for greatly facilitating the catalytic activity of pristine g-C$_3$N$_4$. However, the literature based on the building up 2D/2D Mo$_2$C/g-C$_3$N$_4$ VDW heterojunction for photocatalysis is still absent. In addition, the relationship between photocatalytic performance and physicochemical properties of this VDW heterojunction is worthy to be studied due to it is still in immature stage. Thus, it is significant to investigate the mechanism of photocatalytic process and charge transfer at VDW heterojunction via the combination of theoretical and experimental research.

In this work, a 2D/2D Mo$_2$C/g-C$_3$N$_4$ (MCN) VDW heterojunction is fabricated by electrostatic self-assembly method. To investigate the strong electron interaction between 2D/2D VDW heterojunction, we computationally explored the geometric structure, electronic properties, band edge positions, work function, and charge transfer via first-principles calculation. The Mo$_2$C strongly coordinates with g-C$_3$N$_4$ to

endow g-C$_3$N$_4$ ordered in-plane electron migration and the strong electronic coupling between the VDW forces induces electrons transfer within interlayers. Additionally, the internal electric field between Mo$_2$C and g-C$_3$N$_4$ is established and it synergistically enhances the photocatalytic overall performance, including the higher separation efficiency of electron-hole pairs, the pronged lifetime of photo-induced charge carriers, the lower electrical resistance and the shorter electrons migration distance. We believe that the 2D/2D MCN VDW heterojunction photocatalyst is a viable candidate for the water purification field.

2. Experimental section

2.1. Reagents

2-methylimidazole, molybdenum powder, methanol, cobalt nitrate hexahydrate, hydrogen peroxide (H$_2$O$_2$), disodium oxalate (Na$_2$C$_2$O$_4$), 2,2,6,6-tetramethylpiperidine-1-oxyl (TEMPOL), tert-butyl alcohol (C$_4$H$_{10}$O, TBA) and TC were purchased from Sinopharm Corporation Ltd. (Shanghai, China). In this research, all reagents used were of analytical grade, without need for further purification.

2.2. Synthesis of catalysts

2.2.1. Synthesis of MoO$_3$ nanosheets

The MoO$_3$ nanosheets were synthesized via the previously reported method [28]. In a typical synthetic procedure, 72 mL ethanol and 6 mmol Mo powder were transferred into a Teflon vessel with 9 mL H$_2$O$_2$. Then magnetically stirred for about 30 min to obtain the transparent yellow solution. The Teflon lined stainless steel autoclave was then heated and maintained at 140 °C for 12 h. Then the blue precipitate was filtered and washed with deionized water and ethanol for three times. After dried overnight at 60 °C, the MoO$_3$ nanosheets obtained, shown in Fig. S1.

2.2.2. Synthesis of porous Mo$_2$C nanosheets (Mo$_2$C NS)

For the synthesis of Mo$_2$C NS [29]. First, 1.48 g MoO$_3$ powder and 1.05 g cobalt nitrate hexahydrate was mixture and added 20 mL methanol solution. Then, 3.28 g 2-methylimidazole was dissolved in 20 mL methanol solution and added into above solution. Next, the mixture was stirred for 3 h, filtered and dried overnight to obtain blue products. The obtained blue products were carburized at 800 °C for 3 h at a ramp rate of 5 °C min^{-1}. Finally, the obtained powders were etching in HCl (0.4 M) for 4 h under continuous stirring to remove excess cobalt element and unstable species. The etched samples were then washed with deionized water and ethanol for three times. After dried overnight at 60 °C, the Mo$_2$C NS were obtained.

2.2.3. Synthesis of porous Mo$_2$C nanosheets/g-C$_3$N$_4$ nanosheets (MCN NS) samples

The MCN NS samples were synthesized by a facile electrostatic self-assembly method (Fig. S2). The bulk g-C$_3$N$_4$ was prepared via calcination of melamine at 550 °C for 4 h. Then the yellow product was ground into powder and further heated at 500 °C for 3 h. Thus, the CNS were obtained. 1 g as-prepared CNS was dispersed in 30 mL methanol and ultrasonicated for 30 min. A certain amount of Mo$_2$C NS was added and then continue ultrasound-treated for 1 h to strengthen the interfacial interaction. For building mutual electrostatic attraction, the mixture solution was stirred for 8 h and then the precipitate was filtered and dried. The mass ratios of Mo$_2$C to g-C$_3$N$_4$ were selected as 0.5, 1, 2, 3, 5% and the as-prepared samples were labeled as MCN NS-X (X = 0.5,1, 2, 3, 5).

2.3. Characterization

The structure and surface morphology of samples were observed by a

field emission scanning electron microscope (SEM, Zeiss Gemini 300) and a transmission electron microscope (TEM, USA). The elemental mappings and chemical compositions of the samples were obtained on an energy-dispersive X-ray spectrometer (EDX) equipped on SEM. Atomic force microscopy (AFM) images were acquired on a Dimension Edge (Bruke, Germany). The specific surface area measurements were performed by the Brunauer-Emmett Teller (BET) method (ASAP 2020 HD88, Micromeritics, USA). Fourier transform infrared (FTIR) spectra were obtained by a Bruker Vertex 70 spectrophotometer. The crystal phase of samples was measured by an X-ray diffractometer with Cu Kα radiation (Empyrean, PANalytical B.V). Ultraviolet-visible (UV–vis) diffuse reflection spectra were collected by a UV–vis U-3900H spectrophotometer. The patterns of X-ray photoelectron spectroscopy (XPS) were acquired on a K-Alpha spectrometer (Thermo Scientific, USA). The time-resolved photoluminescence (TRPL) spectra and the Photoluminescence (PL) spectra were collected on a FLS 980 fluorescence spectrophotometer (Edinburgh Instruments, UK).

2.4. Photocatalytic performance evaluation

The photocatalytic activities of the as-prepared MCN NS nanocomposites were evaluated by the experiment of tetracycline (TC) degradation under visible light. The experiment was performed in a 100 mL beaker. The light source was originated from the 300 W xenon lamp (CEL-HXF300, Ceaulight) with the equipment of 420 nm cut-off filter. In a typical reaction, 30 mg MCN NS catalyst powders was dispersed in 50 mL of TC aqueous solution (20 mg L^{-1}). Prior to photocatalytic reaction, the suspension was stirred in the darkness for 1 h to reach the adsorption-desorption equilibrium. The solution samples were withdrawn (3 mL) at a given irradiation time interval and then filtered using 0.25 μm PVDF filter to remove the powder. The concentration of TC was analyzed by a high-performance liquid chromatograph (HPLC, Agilent, Waldbronn, Germany) at detecting λ of 355 nm (The experimental details were provided in Supporting Information). A liquid chromatography coupled with tandem mass spectrometry (LC-MS/MS) system was utilized to identify the transformation products and reaction pathways of TC (The experimental details were provided in Supporting Information). The total organic carbon (TOC) assay was investigated on an analyzer (Shimadzu, TOC-VCPH). To assess the stability of samples, the used catalysts were recycled via centrifugation after one trial, and then washed with deionized water and ethanol for three time, respectively. Then, the recovered samples were dried in an oven and used for cycle experiment. Moreover, to identify the predominant active species generated during the catalytic process, the radical trapping experiments were performed. Tert-butyl alcohol (TBA), disodium oxalate (Na$_2$C$_2$O$_4$) and 4-hydroxy-2,2,6,6-tetramethylpiperidinyloxy (TEMPOL) were utilized to trap hydroxyl radicals (•OH), photo-excited holes (h$^+$) and superoxide radicals (•O$_2^-$), respectively. 10 mM scavengers were added into the suspension during the photocatalytic reaction. The subsequent operations maintained the same steps as the above photocatalytic degradation experiment.

2.5. Theoretical calculation method

All simulations were performed based on the DFT computations, implemented by the Materials Studio 8.0. The geometry optimization calculations were carried out by the Perdew-Burke- Ernzerhof (PBE) in the generalized gradient approximation (GGA) [30]. The cut-off energies for plane-wave expansion were set as 789.1, 381, 789.1 eV for CN, Mo$_2$C and MCN, respectively. We used $1 \times 1 \times 1$ k-point mesh for geometry optimization. An adequately large 15 Å vacuum space was utilized to eliminate the spurious interactions between neighboring systems. The convergence tolerance parameter for the max step size was 0.002 Å, the energy change was 2.0×10^{-5} eV/atom, the maximum stress was 0.1 GPa, and the maximum force was 0.05 eV/Å.

3. Results and discussion

3.1. Structure, morphology, and chemical states analysis

The structures of these samples are analyzed by XRD patterns and FTIR spectra. The XRD spectra clearly demonstrate the successful preparation of β- Mo$_2$C and MCN NS composites, displayed in Fig. 1a. For pure Mo$_2$C, characteristic peaks at 34.35°, 37.97°, 39.39°, 52.12°, 61.52°, 69.56°, 74.64°, 75.51° can be assigned to the (100), (002), (101), (102), (110), (103), (112), (201) planes of the hexagonal β-Mo$_2$C (JCPDF no. 35–0787) [31], respectively. The characteristic peaks at 13.1° and 27.5° are assigned to the (100) and (002) planes of CNS [32]. For the MCN NS specimen, all samples still maintain the characteristic peaks of CNS. With the content of Mo$_2$C increased, the characteristic peaks of Mo$_2$C become distinct, indicating the successful fabrication of MCN NS composites. The molecular structures of CNS and MCN NS are detected through FTIR spectroscopy, shown in Fig. 1b. Obviously, MCN NS samples possess similar peaks comparing to CNS, demonstrating the MCN NS still maintain the basic structure of CNS. The three feature peaks located at 810, 1200–1700, 3000–3500 cm^{-1}, could be ascribed to the stretching vibration of s-triazine subunits, the typical C–N heterocycles and vibration of N–H bonds, respectively [33]. The chemical states and composition of the samples are investigated by XPS. The survey spectrum of MCN NS confirms the presence of molybdenum, carbon, nitrogen and oxygen (Fig. 1c). Fig. 1d shows the C 1s spectra of CNS and MCN NS. The C 1s spectrum of CNS is divided into two peaks (284.6 eV and 288.1 eV), which could be assigned to C–C and N–C=N [34]. Compared to CNS, the binding energies of all C 1s peaks in MCN NS exhibit a positive shift (about 0.3 eV). The N 1s spectra of CNS and MCN NS are provided in Fig. 1e. For CNS, four peaks at 398.6 eV, 399.6 eV, 400.9 eV and 404.3 eV can be detected, corresponding to C=N–C, N–(C)$_3$, C–N–H and charging effects in heterocycles, respectively [35]. Obviously, comparing with CNS, the binding energy of N 1s in MCN NS demonstrates a positive shift of 0.4 eV. The Mo 3d XPS spectra are deconvoluted into 3d3/2 and 3d5/2 peaks due to spin-orbital coupling (Fig. 1f). Peak deconvolution of the Mo 3d spectrum divulges the contribution from Mo$_2$C (d3/2 at 231.5 eV, d5/2 at 228.3 eV), MoO$_2$ (d3/2 at 232.6 eV, d5/2 at 229.2 eV), and MoO$_3$ (d3/2 at 235.4 eV, d5/2 at 232.3 eV) [31]. The presence of superficial oxides is unavoidable for carbide materials upon exposed to air. It worth to noting that the Mo 3d binding energy of MCN NS shows a negative shift comparing with that of Mo$_2$C NS. Nevertheless, the binding energies of C 1s and N 1s in MCN NS both show a positive shift comparing to CNS. These changes demonstrate the strong VDW heterojunction effect between the MCN NS, facilitating the electrons transfer from CNS to Mo$_2$C NS and increasing the electron density of Mo$_2$C NS.

The morphological and elemental composition of Mo$_2$C NS, CNS, and MCN NS were characterized by SEM and TEM. The synthesized Mo$_2$C and CN are nanosheets as expected, as shown in Fig. 2a and b. Fig. S3 shows the SEM images of Mo$_2$C NS at different magnifications. TEM images further demonstrate the porous structure of Mo$_2$C (Fig. 2c) and the typical amorphous 2D ultrathin nanosheet morphology of CN (Fig. 2d). Fig. S4 shows the HRTEM image of Mo$_2$C NS, the inter-planar spacing of Mo$_2$C (0.23 nm and 0.26 nm) can be clearly observed, which is corresponding to the (101) and (100) planes of hexagonal Mo$_2$C [36]. The observation of TEM image for MCN NS-2 (Fig. 2e) shows that the porous Mo$_2$C NS is adhered tightly on the surface of ultrathin CNS. The HRTEM image of MCN NS is displayed in Fig. 2f, it not only shows an amorphous CN, but also the characteristic lattice fringe of 0.23 nm and 0.26 nm in Mo$_2$C can be found. Such an intimate interface between CNS and MCN NS expedites the separation and migration of photo-induced charge carriers and guarantees the stability, thus boosting the photocatalytic activity. We apply the FESEM-EDS elemental mapping (Fig. 2g) and EDX spectra (Fig. S5) to further investigate the elemental distribution. The EDS elemental mapping images clearly reveal the homogeneously distribution of C, N, Mo elements, implying the successfully
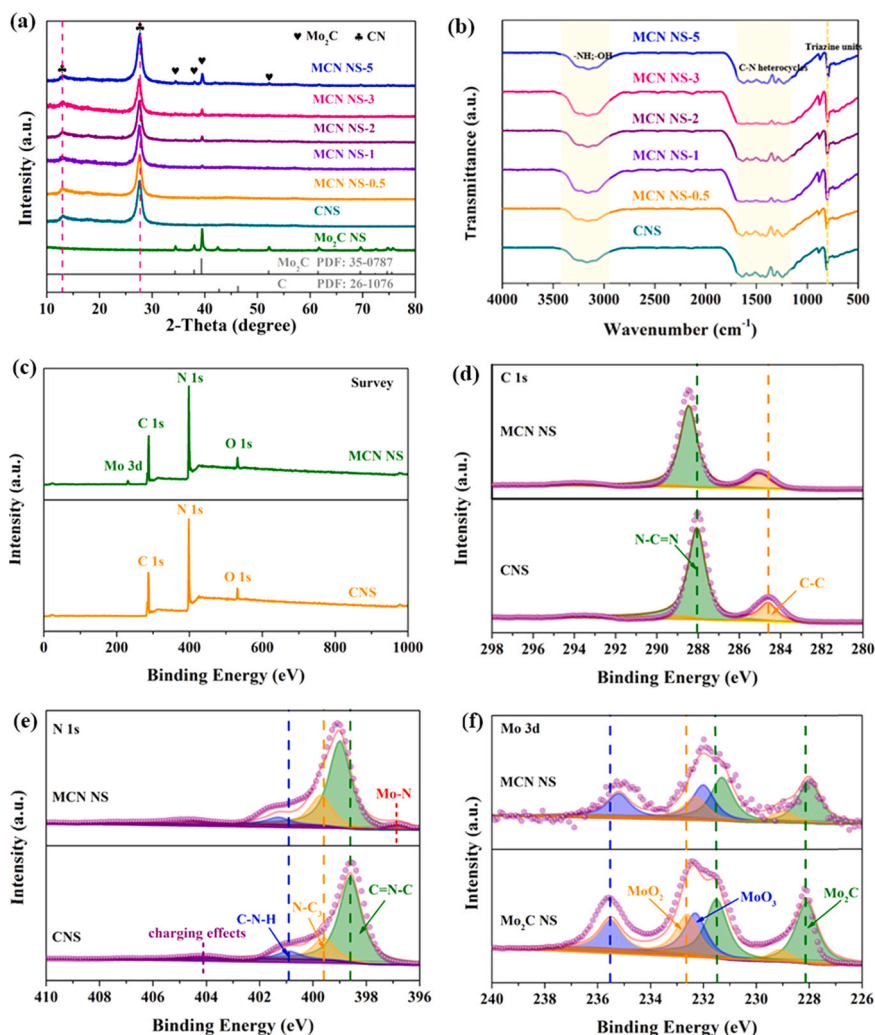
Fig. 1. (a) XRD patterns of Mo$_2$C NS, CNS, and MCN NS samples; (b) FTIR patterns of the samples; XPS patterns of the samples: (c) a total survey, (d) C 1s, (e) N 1s, (f) Mo 3d. Mo$_2$C: green, MoO$_2$: orange, MoO$_3$: blue.

fabrication of MCN NS composite photocatalysts. AFM analysis can furnish specific thickness and size of 2D nanosheets. Fig. 3a-d depict the tapping mode AFM images and the corresponding height distribution profile of Mo$_2$C NS and CNS. As shown in Fig. 3a and b, the Mo$_2$C possesses typical nanosheet structure and the average thickness is about 3.7 nm. AFM image of the CNS sample (Fig. 3c and d) confirms the materials average thickness is about 2.8 nm and presents a clean surface feature, in agreement with the TEM result. The theoretical thickness of CN is around 0.33 nm, manifesting the measured 2D material is few-layer nanosheet [18]. The measured values clearly demonstrate that the thermal stripping technology could convert bulk CN into ultra-thin nanosheets. The converted structures are favorable to expose more active sites and stimulate the speedy electron transport. In addition, the existence of VWD forces formed by this idiographic ultrathin material significantly facilitating the photogenerated charge kinetics, which ascribing to the strong electron coupling effect between CNS and Mo$_2$C NS. In order to investigate the BET specific surface area of the catalysts, the nitrogen adsorption-desorption experiment was performed. As shown in Fig. 3e, both CNS and MCN NS samples possess representative IV adsorption and similar pore size distribution, which represented the features of mesoporous structure. The BET specific surface areas of Mo$_2$C NS, CNS and MCN NS are 13.6, 20.8 and 18.3 m^2/g, respectively. While CNS integrating with Mo$_2$C NS, the BET surface areas of MCN NS reduce slightly, which might originate from the fact that Mo$_2$C NS covering in the surface of CNS during the electrostatic self-assembly process. The

similar adsorption feature, pore size distribution and specific surface area of CNS and MCN NS signify the influence of them on facilitating the photocatalytic activity is negligible.

3.2. Photocatalytic performance and stability

The photocatalytic behavior of the obtained MCN catalysts was assessed by the photodegradation of TC under visible light irradiation. Prior to the light irradiation, the TC solution was stirred for 60 min under dark condition to establish adsorption-desorption equilibrium. Fig. 4a displays the changes in TC concentration (C_t/C_0) of different samples within 60 min irradiation time. The C_0 refers to the initial concentration of TC and the C_t represents the t-time concentration of TC. As displayed in Fig. 4a, the natural photolysis of TC solution was negligible. The CNS and Mo$_2$C NS exhibit dispiriting TC removal efficiency, which are merely 64% and 45% within 1 h, respectively. The Mo$_2$C exhibited excellent adsorption properties for the target contaminants, maybe attributing to the Mo element in Mo$_2$C. The transition metal atoms could provide valence electrons and cause more adsorptive sites [37], facilitating the adsorption of pollutants. Thus, with the content Mo$_2$C of increasing, the adsorption capacity of the MCN composite increased. The excellent property is conducive to the accumulation of pollutants to the catalytic active center, so more active substances can flow smoothly to the pollutants, resulting in the degradation of pollutants into H$_2$O and CO$_2$ [38]. The degradation efficiencies of the MCN NS
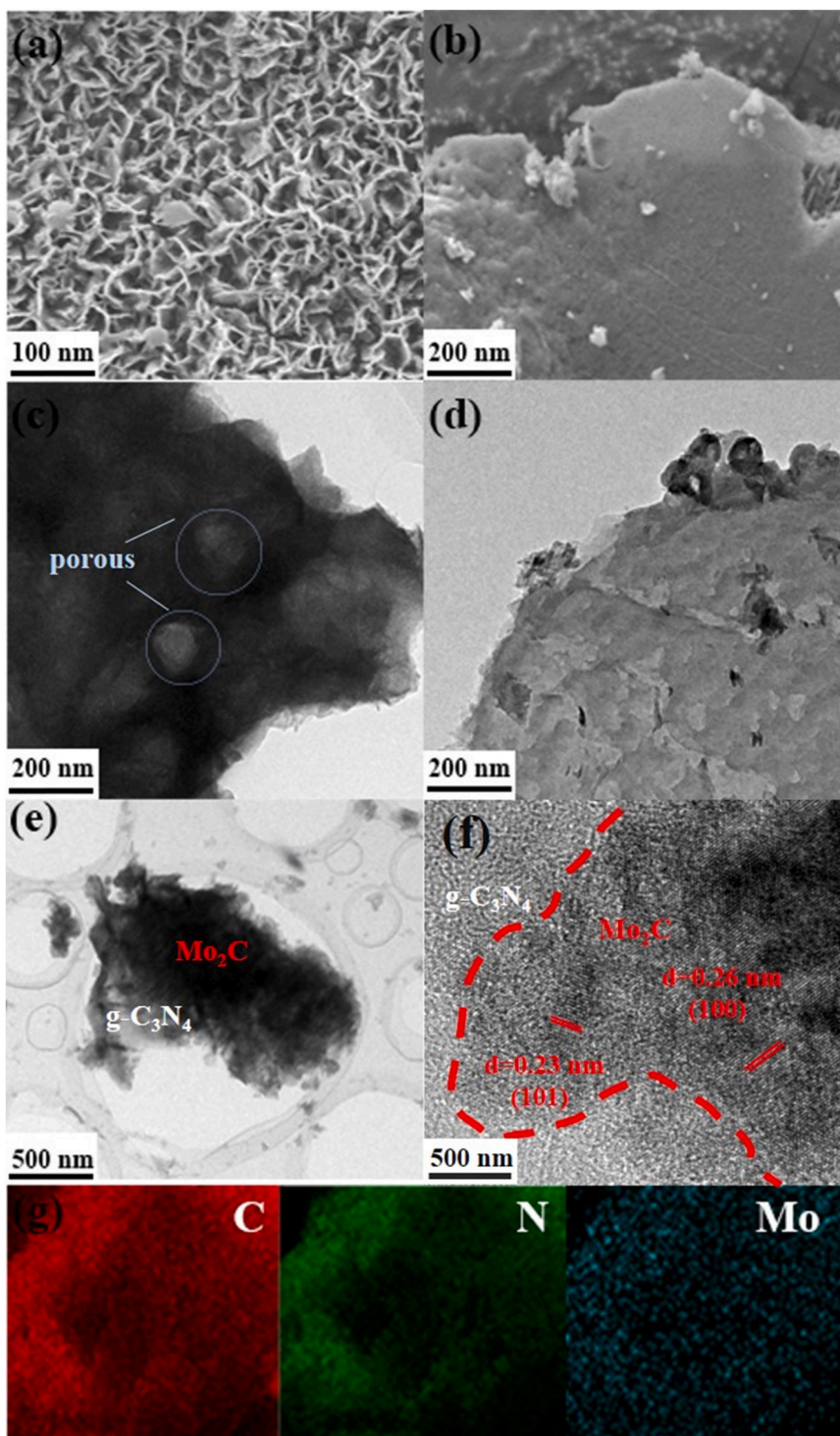
Fig. 2. SEM images of (a) Mo_2C NS, (b) CNS; TEM images of (c) Mo_2C NS, (d) CNS, (e) MCN NS; (f) HRTEM image and (g) FESEM-EDS elemental mapping of MCN NS.

samples are all significantly higher than that of the CNS and Mo_2C NS. For comparison, the degradation efficiency of the bulk CN samples is displayed in Fig. S6. With an increasing mass ratio of Mo_2C, the photocatalytic degradation activity of MCN NS presents an increasing trend. The MCN NS-2 gains its highest degradation efficiency (97%) with the optimized mass ratios of Mo_2C at 2 wt%, but the sequentially adding of Mo_2C volumes will lead to the degradation of catalytic performance, corroborating the mass ratio of the Mo_2C and CN greatly affects the photocatalytic performance. An excess Mo_2C can shelter the reaction

active spots and introduce new recombination centers [31]. To further investigate the reaction rate of photocatalysis, the apparent rate constant (k) is obtained, as the following equation:

$$k = \frac{\ln(C_0/C)}{t} \tag{1}$$

As shown in the kinetic curves (Fig. 4b), the k values conform the order: MCN NS-2 (0.066)> MCN NS-1 (0.055)> MCN NS-3 (0.051)> MCN NS-5 (0.037)> MCN NS-0.5 (0.031)> CN NS (0.017). The MCN
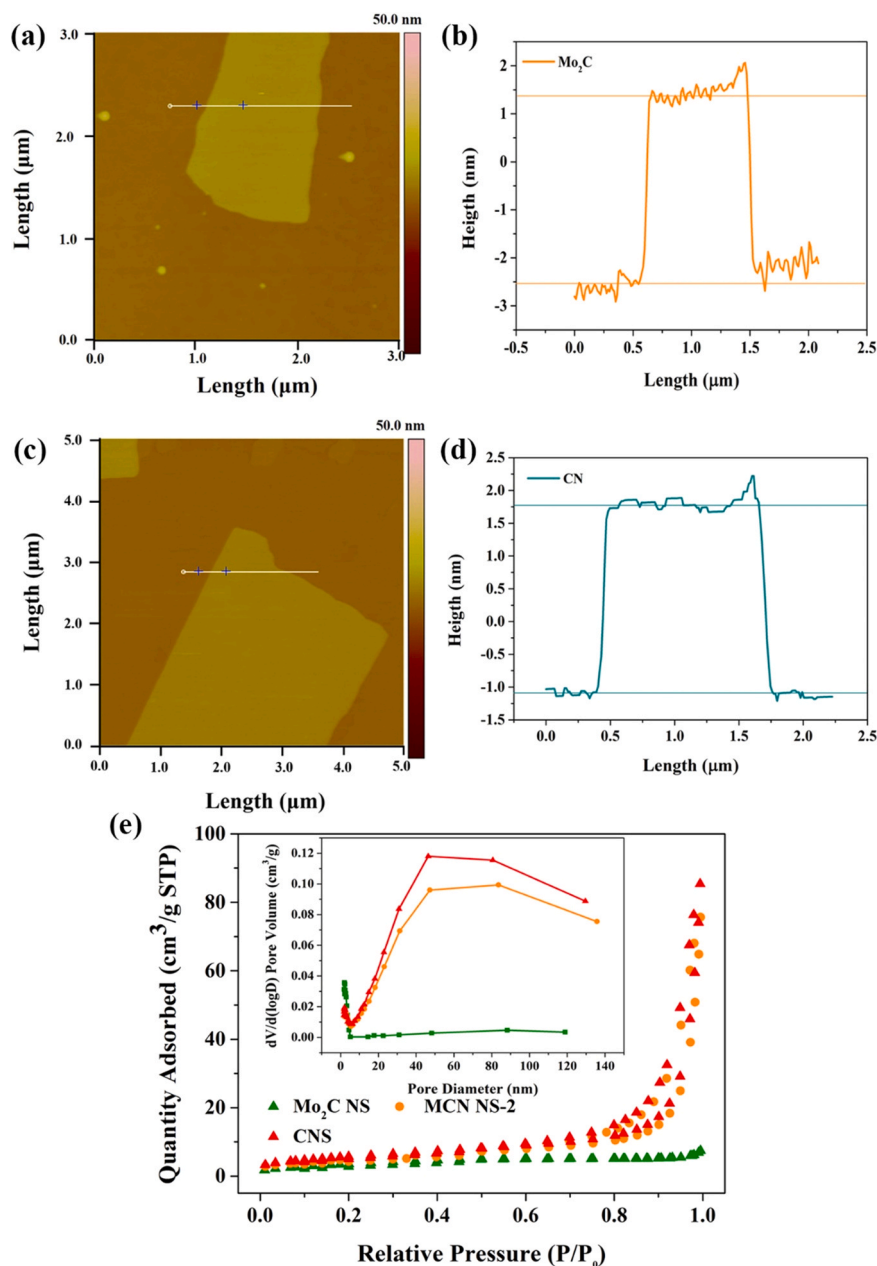
Fig. 3. (a) AFM image and (b) cross-section profile of Mo$_2$C NS; (c) AFM image and (d) cross-section profile of CNS; (e) Nitrogen adsorption-desorption isotherms and the pore size distribution curves (insert) for Mo$_2$C NS, CNS and MCN NS-2.

NS-2 possesses the highest apparent rate constant, which is about 3.9 times higher than that of CNS. The coplanar stacking between ultrathin CN nanosheet and porous Mo$_2$C nanosheet causes the localization of electrons in the nano-interfaces between 2D VDW heterostructure and the strong interaction is favorable to the transfer of electrons, thus effectively accelerating the charge separation. The complete degradation of pollutants into H$_2$O and CO$_2$ is essential for removing environmental pollution. Thus, we deeper evaluate the ability of MCN NS-2 to mineralize organic pollutants. The mineralization property is analyzed by a TOC analyzer. As shown in Fig. 4c, the mineralization efficiency (TOC$_t$/TOC) of TC by MCN NS-2 photocatalysts reaches to 76% within 2 h visible light irradiation. The TOC$_t$ represents the TOC value at time t and the TOC$_0$ refers to the initial TOC value of TC. The high mineralization efficiency demonstrates the strong ability of MCN NS-2 to decompose organic pollutants into substances that are environmental harmless. For the aim of refraining from secondary pollution and saving costs, the recyclability and excellent chemical stability of photocatalysts

are also an important property. The stability of MCN NS-2 is evaluated through a cycle experiment. As shown in Fig. 4d, after four-round continuous reaction, the MCN NS-2 still exhibits high degradation efficiency with little inhibition. The recyclability and stability could provide great prospects for practical applications. Furthermore, after four reaction cycles, the used MCN NS-2 photocatalyst is characterized by XRD and FTIR (Fig. 4e and f). The spectra of fresh sample and used sample remain almost unchanged, further verifying the physicochemical stability and the chemical structures of MCN NS-2 are not destroyed after photocatalytic reaction. Meanwhile, the photocatalytic activity of MCN NS-2 is higher than most of other g-C$_3$N$_4$ based photocatalysts reported previously (Table 1), manifesting that MCN NS is an efficient photocatalysts for pollutants degradation.

Furthermore, the generation of various oxidative species over the MCN NS-2 photocatalysts is probed by the 5, 5-dimethyl-1-pyrroline N-oxide (DMPO) spin-trapping electron spin resonance (ESR) technique and reactive species trapping experiments. From the results of Fig. 4g
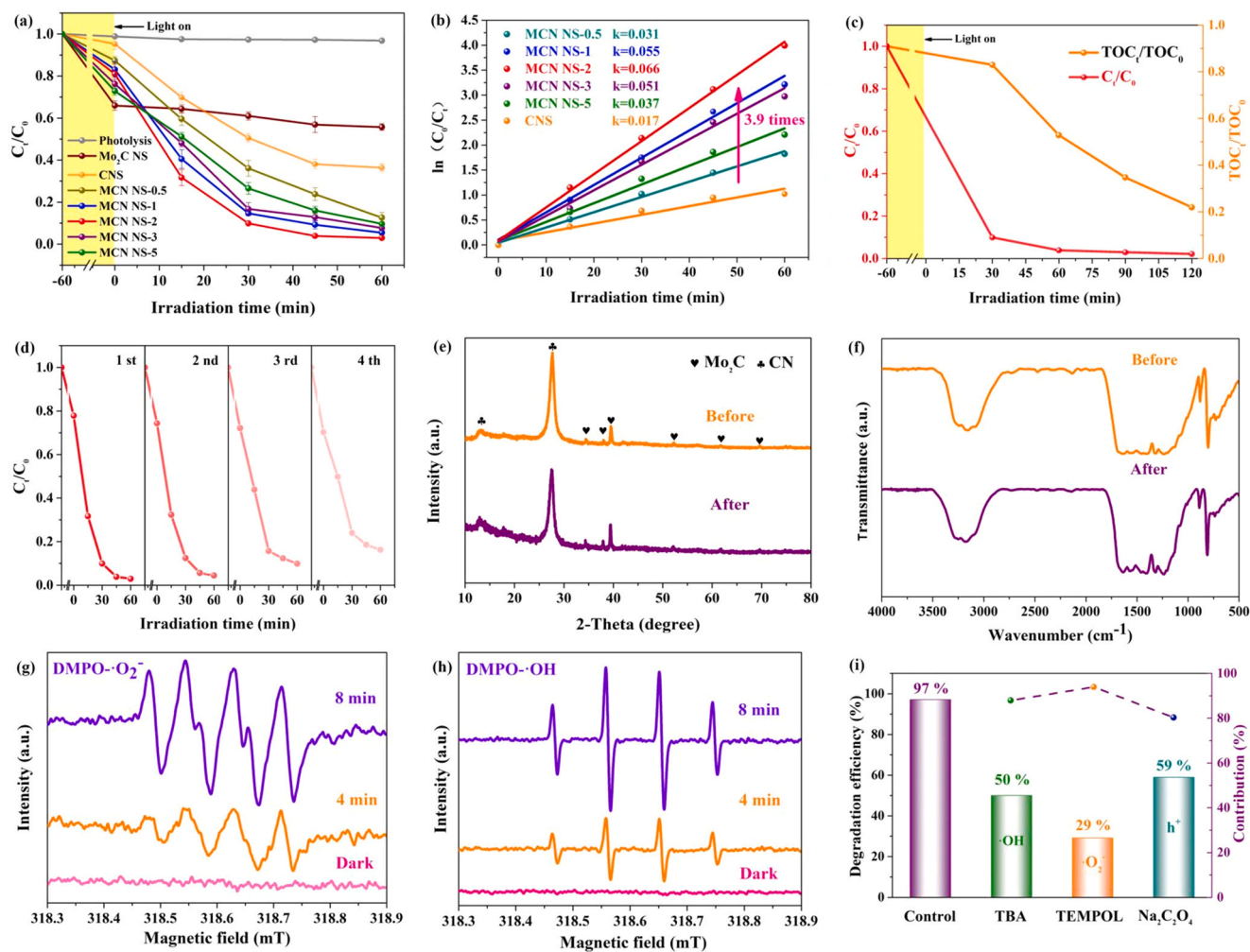
Fig. 4. (a) Photocatalytic degradation efficiency of TC over different samples under visible light irradiation (λ > 420 nm). (b) Pseudo-first-order kinetic fitting curves and the corresponding kinetic constants. (c) The photocatalytic degradation and TOC removal curves of TC on MCN NS-2 photocatalysts. (d) The cycling test for the degradation of TC by the fresh and used MCN NS-2 catalysts. (e) XRD, (f) FTIR for MCN NS-2 photocatalyst before and after used. ESR spectra of the (g) DMPO-•O_2^- adduct, (h) DMPO-•OH adduct for MCN NS-2 under visible light irradiation. (i) Photocatalytic degradation efficiencies of TC under visible light irradiation (λ > 420 nm) over MCN NS-2 photocatalyst with different quenchers.

Table 1
Comparison with other g-C_3N_4 based photocatalysts for degradation.

Photocatalysts	Pollutant concentration (mg L^{-1})	Dosage (g L^{-1})	Light source	K[a] (min^{-1})	Refs. (year)
TiO_2/g-C_3N_4	TC(15)	0.6	300 W X[c] (λ > 400 nm)	0.024	[39] (2020)
Ag/g-C_3N_4	TC(20)	1.67	300 W XL (λ > 400 nm)	0.012	[40] (2020)
Co-pCN	OTC[b] (20)	0.3	300 W XL (λ > 420 nm)	0.038	[35] (2020)
BPTCN[d]	OTC (10)	0.6	300 W XL (λ > 420 nm)	0.026	[32] (2020)
WO_3/g-C_3N_4	TC(20)	1	300 W XL (λ > 420 nm)	0.038	[41] (2020)
2D/3DCN/CC[e]	TC(10)	0.5	250 W XL (λ > 420 nm)	0.01	[42] (2020)
MCN NS	TC(20)	0.6	300 W XL (λ > 420 nm)	0.066	This work

[a] k is apparent rate constant;
[b] OTC is oxytetracycline;
[c] XL is the xenon lamp;
[d] BPTCN: black phosphorus (BP) decorated on the tubular g-C_3N_4 (TCN);
[e] 2D/3D CN/CC: 3D g-C_3N_4 (3D CC) microspheres tightly anchor on the surface of 2D g-C_3N_4 (2D CN) nanosheets.

and h, no ESR signals are detected under dark conditions (0 min), but the intensity of ESR signals increased dramatically under visible light irradiation (4 min and 8 min). The intensity ratios of 1:1:1:1 and 1:2:2:1 correspond to the DMPO-•O_2^- and DMPO-•OH adducts, respectively. As the irradiation time prolonged, the signal intensity of DMPO-•O_2^- adducts increased, which is ascribing to the increased concentration of free electrons, thus continuously stimulating the production of •O_2^-.

Meanwhile, the variation trend of DMPO-•OH signal is consistent with DMPO-•O_2^-, which means that plentiful reactive species are produced under light irradiation. In order to determine the major active species generated in the MCN NS-2 photo-degradation system, scavenging experiments are performed by adding quenchers. Hence, TEMPOL, $Na_2C_2O_4$ and TBA were executed as quenchers of •O_2^-, holes (h$^+$) and hydroxyl radicals (•OH), respectively [32,34]. As shown in Fig. 4i, the

main reactive species are $\bullet O_2^-$, $\bullet OH$ and h^+ during the photo-degradation reaction process for MCN NS-2. The degradation efficiency of TC after 60 min visible light irradiation are 29%, 50% and 59% (Fig. 4i and Fig. S7), corresponding to the quenchers of TEMPOL, TBA and $Na_2C_2O_4$, respectively. And the corresponding k values are 0.004, 0.008 and 0.013 min^{-1}, respectively (Fig. S7). The relative contributions of h^+, $\bullet OH$ and $\bullet O_2^-$ to the overall TC photodegradation kinetics can be deduced by following equations [35]:

$$R_{h^+} = \frac{k_{h^+}}{k} \approx \frac{k - k_{Na_2C_2O_4}}{k} \qquad (2)$$

$$R_{\bullet OH} = \frac{k_{\bullet OH}}{k} \approx \frac{k - k_{TBA}}{k} \qquad (3)$$

$$R_{\bullet O_2^-} = \frac{k_{\bullet O_2^-}}{k} \approx \frac{k - k_{TEMPOL}}{k} \qquad (4)$$

Accordingly, the relative contributions of h^+, $\bullet OH$ and $\bullet O_2^-$ to the TC removal are calculated to be 80.3%, 87.9% and 93.9% respectively. Due to the convoluted radical chemistry involved in the photocatalytic process, the sum of these contributions exceeds 100%. These results demonstrate that $\bullet O_2^-$, $\bullet OH$ and h^+ play significant roles in the MCN NS-2 photocatalytic TC degradation system. The advantages of MCN NS-2 in boosting transfer efficiency of electrons are fully demonstrated. The abundant active species detected in the photocatalytic system can be attribute to the strong electron coupling effect in the 2D/2D VDW heterojunction, stimulating the photogenerated charge kinetics and providing massive reactive centers to facilitate the degradation reaction.

To further investigate the structure transformation mechanism of TC during the photocatalytic process, the photocatalytic intermediates and reasonable photo-degradation pathway are identified by the LC-MS/MS technique. The MS spectra of the TC solution after 1 h irradiation, molecular weights and molecular structural formulas of the intermediate products are shown in (Fig. S8 and Table S1). According to the LC-MS/MS results and literatures reported previously, the possible degradation paths are depicted in Scheme 1. The mass-to-charge ratio (m/z) of 445 is identified as protonated tetracycline molecule (TC-H^+) [41]. As the irradiation time increased, the prominent peak at $m/z = 445$ becomes lower and lower, and other new peaks with low m/z values are generated. Intermediate product TC 1($m/z = 461$) is derived from the hydroxylation of TC under the attack of $\bullet OH$ [43]. TC 1 is then fragmented into TC 4 ($m/z = 262$) via the deamidation reaction, demethylation reaction and ring-open reaction. With the loss of methyl, hydroxyl group and carbonyl group, the TC 4 is decomposed to TC 5 ($m/z = 216$) [42]. Meanwhile, TC also can be transformed to TC 2 ($m/z = 431$) and TC 3 ($m/z = 417$) via the loss of N-methyl group [10]. On the one hand,

Intermediate product TC 2 can be attacked by h^+ radicals, and degraded via dehydration reaction and ring-opening reaction, leading to the formation of product TC 6 ($m/z = 301$) and further decomposed to TC 7 ($m/z = 287$) [41,44]. The molecular ion product TC 8 ($m/z = 279$) is stemmed from TC 7 via decarboxylation. On the other hand, TC 3 molecules undergo the elimination and deamidation reaction under the contact with $\bullet O_2^-$ and h^+ to yield a new intermediate TC 9 ($m/z = 362$) [45]. Intermediate TC 10 with m/z of 318 can be generated from breaking cyclic hydrocarbon structure of TC 9. Another part of TC 9 is transformed to TC 6 through the dehydration reaction, ring cleavage and losing of methyl or hydroxyl groups. With the oxidization of six membered ring structure in TC 10, TC 11 ($m/z = 239$) is further generated [10]. Subsequently, the intermediates are further oxidized and generate opening ring products including TC 12 ($m/z = 133$), TC 13 ($m/z = 137$), TC 14 ($m/z = 89$) [41,46]. Finally, the above organic intermediates are mineralized to H_2O, CO_2, and other inorganic substances. Moreover, the result is consistent with the variation of high-performance liquid chromatograph and the TOC analysis, where TC molecules are decomposed into small molecules. The MCN NS VDW heterojunction can generate much active radicals as h^+, $\bullet OH$ and $\bullet O_2^-$ to attack the TC molecules, demonstrating ultra-high mineralization ability, thereby improving the removal efficiency of TC.

3.3. Photo-induced charge carrier dynamics

The separation and transfer behaviors of charge carriers are explored through a series of photo-electrochemical characterization techniques. Fig. 5a shows the transient photocurrent density curves of CNS and MCN NS on the typical cycles of visible light on or off. The photocurrent response curves are interrelating with the photo-induced charge separation ability of these samples. Upon the light on, the transient photocurrents generate immediately, manifesting the strong photo-sensitivity and highly efficient spatial charge migration rate of samples. The saturated photocurrent density of MCN NS (about 0.45 $\mu A\ cm^{-2}$) is bigger than that of CNS (about 0.29 $\mu A\ cm^{-2}$), demonstrating the photo-induced charge carriers separate and transfer more efficiently after incorporating with Mo_2C. To further confirm it, the electrochemical impedance spectra (EIS) are measured to investigate the charge transfer dynamics. The smaller arc in the EIS Nyquist plots corresponds to the lower resistance and better electrical conductivity [13]. As shown in Fig. 5b, the arc radius of the obtained catalysts is in the order of CNS > MCN NS-2 > Mo_2C NS. The Mo_2C NS presents an obvious decrease in the arc radius, implying the ultrahigh electrical conductivity of Mo_2C NS [47]. In the MCN NS VDW hetero-interface, Mo_2C NS minimizes the charge transport resistance and provides powerful driving forces to induce the charges transfer. In addition, for the MCN NS VDW
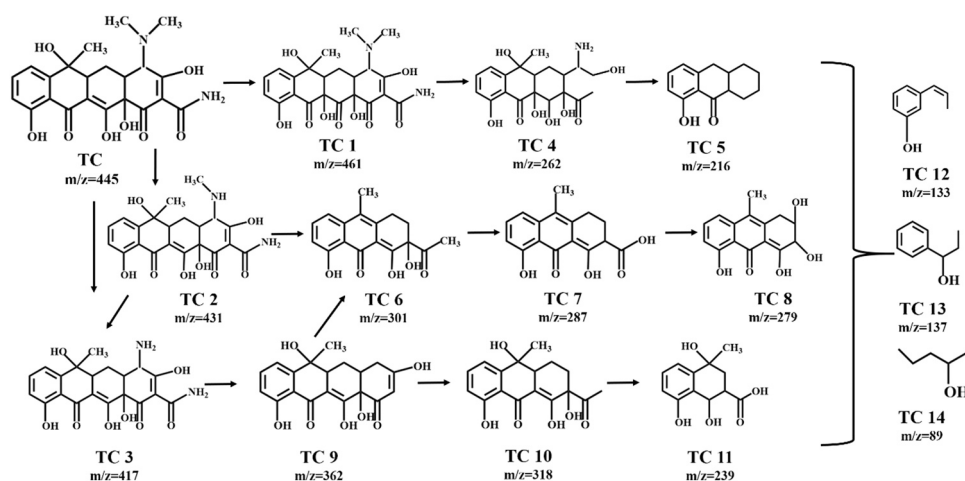
Scheme 1. The possible intermediates and pathways of TC molecule during degradation reaction process.
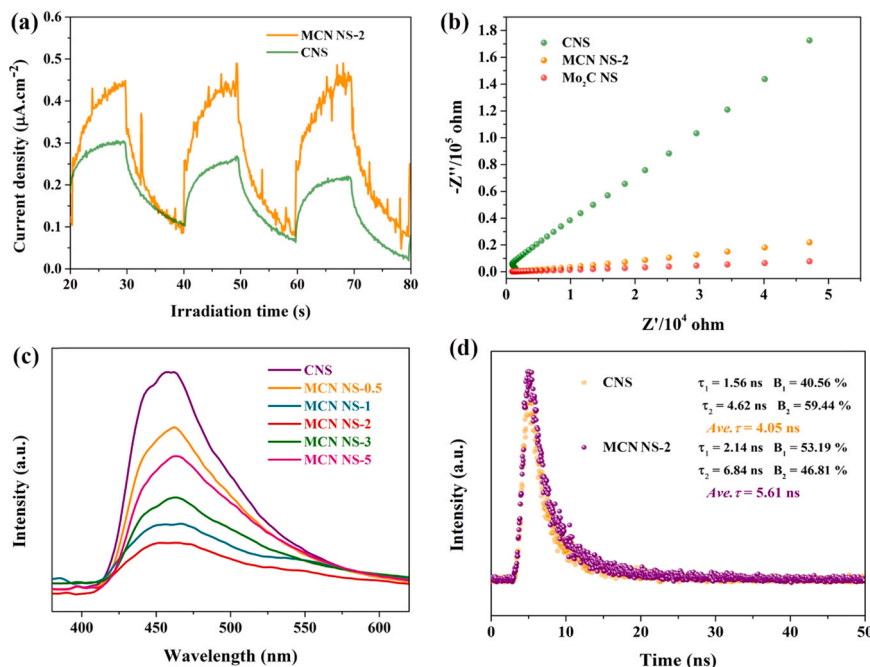
Fig. 5. (a) Transient photocurrent response curves, (b) electrochemical impedance spectra, (c) photoluminescence spectra and (d) time-resolved photoluminescence spectra of the samples.

heterojunction, the distinct "face to face" contact minimizing the migration distance of electrons and providing strong interactions between layers. The spatial charge separation behavior is investigated by the PL technique (Fig. 5c). Under the light excitation of 320 nm wavelength, the CNS shows a strong luminescence emission signal, indicating the radiative recombination of charge carriers. The PL peak decreases dramatically for MCN NS samples, which manifesting the faster spatial charge separation. The lower PL peaks of MCN NS samples might be ascribe to the strong electron coupling effect between the hetero-interface, thus stimulating the charge kinetics. The TRPL decay curves can provide reliable basis for quantitatively analyzing the photo-induced charge carriers lifetimes of CNS and MCN NS. The TRPL spectra of them are probed by the biexponential decay function:

$$R(t) = B_1 exp(-t/\tau_1) + B_2 exp(-t/\tau_2) \tag{5}$$

Where τ_1 and τ_2 are the short and long fluorescent lifetime, B_1, B_2 are the pre-exponential factor, respectively. The average longevity (Ave.τ) is obtained by the following equation:

$$Ave.\tau = \frac{B_1\tau_1^2 + B_2\tau_2^2}{B_1\tau_1 + B_2\tau_2} \tag{6}$$

The corresponding carrier dynamics information and lifetime profile of the prepared photocatalysts are displayed in Fig. 5d. The average fluorescent lifetime of CNS and MCN NS-2 are 4.05 ns and 5.61 ns, respectively. The increased lifetime in MCN NS-2 signifies the enhanced electrons transfer rate, thus potentially improving the photocatalytic performance. These results verify the emergence of high-speed electron transfer channels in the 2D/2D VDW heterojunction. The combination of porous Mo_2C NS and CNS could result in the satisfactory transfer of photo-induced electrons. In addition, the increase in Ave.τ of composite photocatalysts is principally ascribed the fact that the Mo_2C serves as electrons trap to enlarge the lifetimes of charge carriers and inhibit the recombination of electron-holes pairs.

3.4. VDW heterojunction (Density functional theory computational calculations)

To investigate the optical properties of MCN NS VDW heterostructure, the UV–vis DRS spectra are performed, as shown in Fig. 6a. The absorption edge of CNS appears at around 450 nm, while Mo_2C exhibits strong photo-absorption in the wavelength range of 300–800 nm. Compared with pure CNS UV–vis DRS, the much-enhanced light absorption for MCN NS is observed over the visible range of 420–800 nm, implying the efficient sensitization effect of Mo_2C on CNS. After hybridization with Mo_2C, the light-harvesting ability of MCN NS increases significantly, which plays a pivotal role in achieving solar energy conversion. The band gaps of CNS and Mo_2C NS can be estimated from the Tauc plots, which are derived using the Kubelka-Munk method [48]. The corresponding band gap energies (E_g) values of CNS and Mo_2C NS can be estimated to be 2.44 and 1.26 eV, which are exactly matched the literature values [32,49]. To further analyze the band structure, the Mott-Schottky plots are employed. Fig. 6c displays the Mott-Schottky plots of CNS and Mo_2C NS within frequencies of 500 Hz and 1000 Hz. The measured positive slopes imply that both Mo_2C NS and CNS are n-type semiconductors [50,51]. The flat band potentials (E_{fb}) of Mo_2C NS and CNS are respectively estimated to be − 0.71 and − 1.31 eV vs. Ag/AgCl (i.e., −0.51 and −1.11 eV vs. normal hydrogen electrode, NHE). Generally, the conductive band (CB) of n-type semiconductor is about 0.2 eV more negative than E_{fb} [26]. Thus, the CB edge potentials (E_{VB}) for Mo_2C NS and CNS are about − 0.71 and − 1.31 eV vs. NHE. The valence band (VB) potentials (E_{VB}) of Mo_2C NS and CNS are 0.55 and 1.13 eV vs. NHE, according to the equation: $E_{VB} = E_{CB} + Eg$. The calculated E_{VB} and E_{CB} edge positions of Mo_2C NS and CNS are summarized in Table S2. After simulation calculation, the optimized geometric structures of Mo_2C NS, CNS and MCN NS can be observed, as shown in Fig. 6d-f. The rectangle lattice constants of these samples are displayed in Table S3.

To further explore the innate character of the strong electronic interaction between Mo_2C NS and CNS, a series of DFT calculations are performed. First, the electrostatic potentials of CNS, Mo_2C NS and MCN NS are exhibited in Fig. 7a-c. The work function is defined to be the minimum energy required for removing an electron from the surface. For probing the interface charge transfer, the surface work function can be used as a dependable basis. The calculation formula is: $\Phi = E_{vacuum} - E_F$ [30]. Among them, E_{vacuum} represents the energy of the electrostatic potential for immobile electrons in vacuum and E_F denotes the
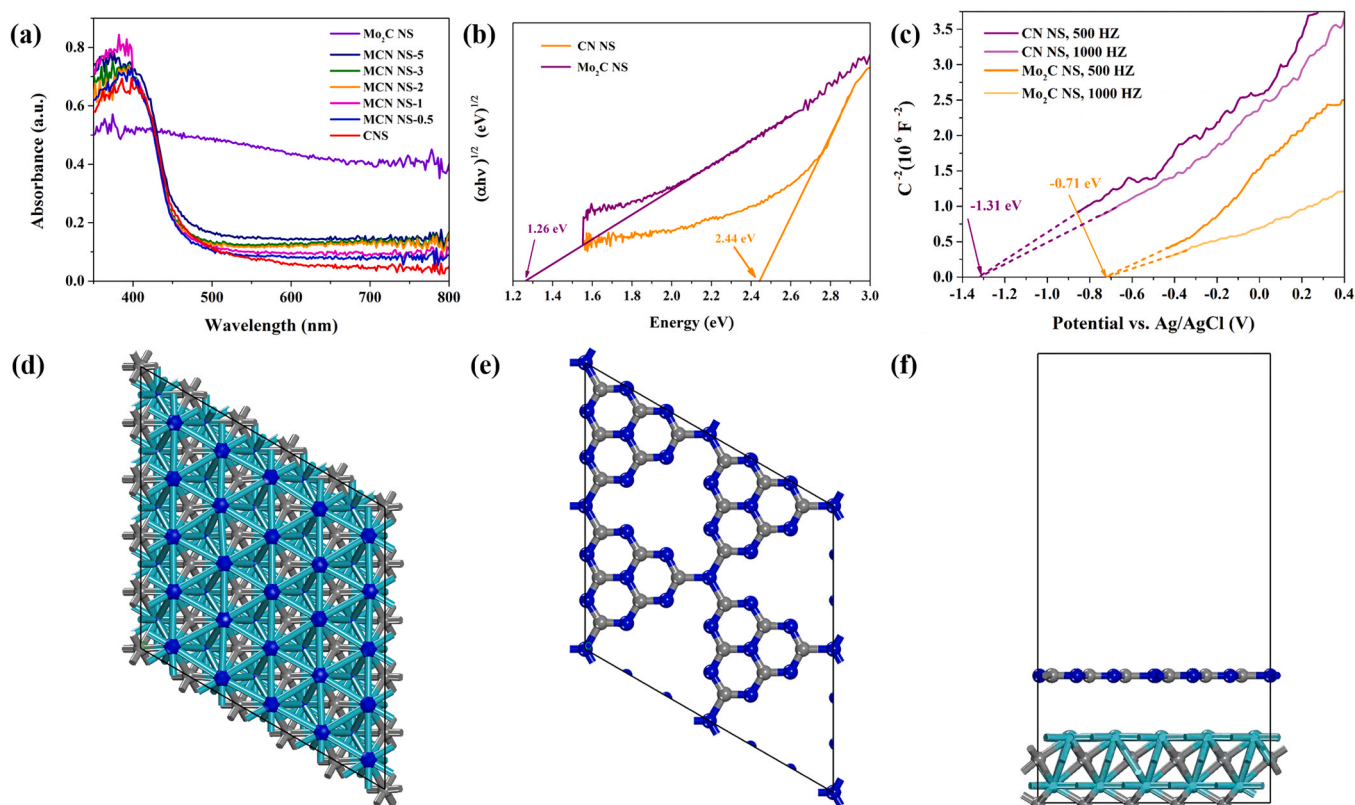
Fig. 6. (a) UV–vis diffusion reflection spectra of CNS, Mo$_2$C NS and MCN NS samples; (b) Tauc plots, (c) Mott-Schottky plots of CNS and Mo$_2$C NS samples; the optimized geometric structures of (d) CNS, (e) Mo$_2$C NS and (f) MCN NS, and the green, gray and blue represent Mo, C and N atoms, respectively.
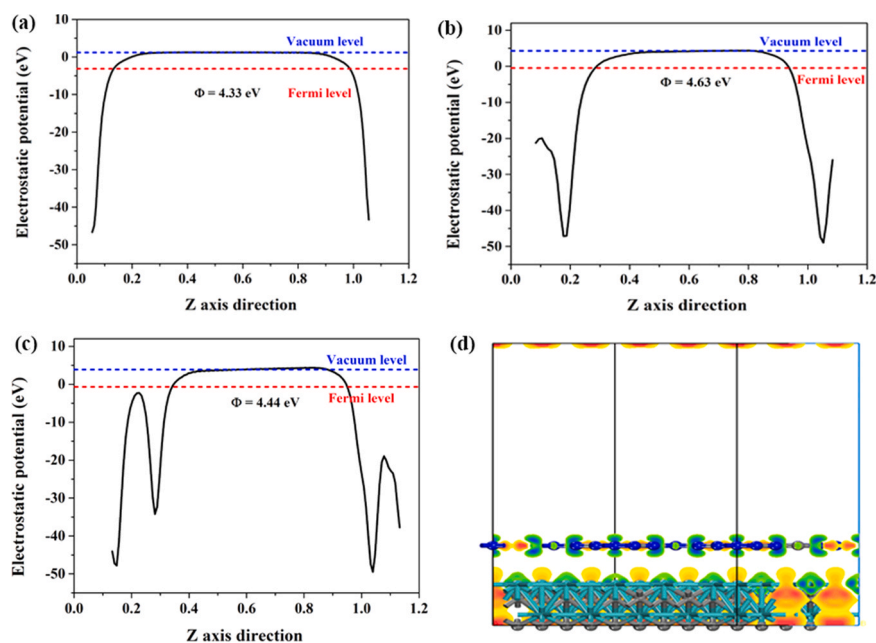

Fig. 7. Average potential profile along Z-axis direction for (a) CNS, (b) Mo$_2$C NS and (c) MCN NS; (d) side-view differential charge density map of CNS and Mo$_2$C NS (The yellow and green regions represent net electron accumulation and depletion, respectively. The green, gray and blue represent Mo, C and N atoms, respectively.).
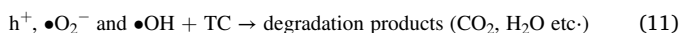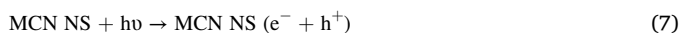
Fermi energy. The work function of CNS, Mo$_2$C NS and MCN NS are calculated to be 4.33, 4.63 and 4.44 eV, respectively, which manifesting the higher Fermi level position of CNS than that of the Mo$_2$C NS. Hence, the higher Fermi potential will drive the electrons to move from the CN layer to Mo$_2$C NS until the E$_F$ tends to be uniform. In addition, the differential charge density of MCN NS VDW heterojunction system is also

calculated. As shown in Fig. 7d, the green and yellow iso-surfaces represent the region of net electron depletion and accumulation respectively. Visibly, a crowd of electrons accumulate at the interface. The surface of Mo$_2$C extracts electron density from adjacent CN, further corroborating the strong electron coupling between MCN NS VDW heterojunction. The charge is depleted on the N atoms, while electrons

accumulate on the Mo atoms. As a result, the layer Mo_2C obtains electrons and acts as an electron acceptor originating from CN. The large potential differences between Mo_2C and CN monolayer will trigger the spontaneous interfacial charge transfer to establish a strong internal electric field in 2D/2D MCN NS VDW heterojunction, and the direction of the built-in electrical field is from CN to Mo_2C and is perpendicular to the heterojunction. Consequently, the excitonic behavior of the 2D/2D MCN NS VDW heterojunction can be quite different from the isolated Mo_2C and CN layers. The gradient of potential across the hetero-interface may accelerate the separation of photo-induced charges. All the above results are consistent with the measured values of XPS. The strong electronic coupling is constructed in MCN NS VDW heterojunction, which is demonstrated by the theoretical computations results and mentioned experiments.

3.5. The possible photocatalytic mechanism

Based on the above theoretical and experimental results, the mechanism for the degradation of TC in the 2D/2D MCN NS VDW heterojunction photocatalyst can be proposed, as presented in Fig. 8. As mentioned in the potential profile, the work functions of Mo_2C NS ($e\Phi_{Mo2C}$) and CNS ($e\Phi_{CN}$) are determined to be 4.63 and 4.33 eV, respectively. When Mo_2C NS and CNS are in contact, the CNS with higher Fermi level position will induce the electrons transfer from CNS to Mo_2C NS until the fermi level between CNS and Mo_2C NS is equilibrated. Thus, the electrons accumulate at the interface and form a large potential difference. Naturally, a space charge layer is generated, leading to the formation of energy barrier, and furnishing formidable driving force for electrons transfer. Consequently, the electrons trapped by Mo_2C NS can not flow back to the CB band of CNS. In this way, the photo-induced charges carriers could be effectively separated. Furthermore, as an electron trap, Mo_2C can transport multitudinous electrons to active species, resulting in a steady stream of active free radicals and realizing the efficient degradation of pollutants. Fig. S9 shows the concentration of H_2O_2 detected by the test paper. Therefore, our proposed strategy for constructing 2D/2D VDW heterojunction is reliable. The possible pollutants degradation reactions of 2D/2D MCN NS VDW heterojunction under visible light irradiations are shown in the following:

$$MCN\ NS + h\upsilon \rightarrow MCN\ NS\ (e^- + h^+) \tag{7}$$

$$O_2 + e^- \rightarrow \bullet O_2^- \tag{8}$$

$$\bullet O_2^- + e^- + 2H^+ \rightarrow H_2O_2 \tag{9}$$

$$H_2O_2 + e^- \rightarrow \bullet OH + OH^- \tag{10}$$

$$h^+, \bullet O_2^-\ and\ \bullet OH + TC \rightarrow degradation\ products\ (CO_2, H_2O\ etc\cdot) \tag{11}$$

4. Conclusion

In conclusion, we have successfully designed and fabricated an interfacial 2D/2D VDW heterojunction of porous MCN NS nanosheets via the electrostatic self-assembly technique. Benefitting from the constructed VDW heterostructure and the oriented charge flow, as verified by both theoretical computations and characterized technologies, the photo-induced charge carriers of MCN NS can be effectively separated and transferred. This 2D/2D MCN NS VDW heterojunction exhibits enviable visible-light photocatalytic for TC degradation. The TC degradation efficiency for optimal sample (MCN NS-2) surprisingly reaches up to 97% and it demonstrates high mineralization efficiency and chemical stability. The apparent rate constant of TC degradation is also as high as 0.066 min^{-1}, which is about 3.8 times than that of CNS. Such improved photocatalytic activity may arise from the large 2D/2D contact interface and the build-in electric field, stimulating the photogenerated charge kinetics. The Mo_2C acts as photosensization unit to strengthen the light
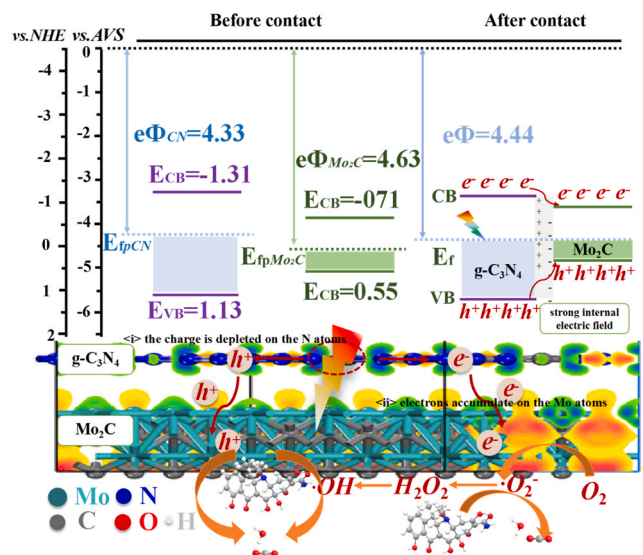

Fig. 8. The photocatalytic mechanism of the 2D/2D MCN NS VDW heterojunction system.

absorption capacity and serves as electron trap to elongate the lifetime of charge carriers. This work not only demonstrates the immense potential of Mo_2C in photocatalysis but also affords the specimen for otherwise fabrication and design of 2D/2D VDW heterojunctions toward the broad potential applications, e.g., catalysis, photovoltaic cells, photodetectors and so on.

CRediT authorship contribution statement

Yin Zhou: Conceptualization, Methodology, Data curation, Writing – original draft. **Chen Zhang**: Supervision, Project administration, Funding acquisition, Writing – review & editing. **Danlian Huang**: Resources, Supervision. **Wenjun Wang**: Validation, Data curation, Writing – review & editing. **Yunbo Zhai**: Resources, Funding acquisition, Project administration. **Qinghua Liang**: Formal analysis. **Yang Yang**: Data curation, Writing – review & editing. **Suhong Tian**: Data curation. **Hanzhuo Luo**: Data curation. **Deyu Qin**: Writing – review & editing.

Declaration of Competing Interest

The authors declare that they have no known competing financial interests or personal relationships that could have appeared to influence the work reported in this paper.

Appendix A. Supporting information

Supplementary data associated with this article can be found in the online version at doi:10.1016/j.apcatb.2021.120749.

References

[1] R.R. Solis, F.J. Rivas, A.M. Chavez, D.D. Dionysiou, Peroxymonosulfate/solar radiation process for the removal of aqueous microcontaminants. Kinetic modeling, influence of variables and matrix constituents, J. Hazard. Mater. 400 (2020), 123118.

[2] S. Li, X. Ao, C. Li, Z. Lu, W. Cao, F. Wu, S. Liu, W. Sun, Insight into PPCP degradation by UV/NH$_2$Cl and comparison with UV/NaClO: kinetics, reaction mechanism, and DBP formation, Water Res. 182 (2020), 115967.

[3] F. Huang, Z. An, M.J. Moran, F. Liu, Recognition of typical antibiotic residues in environmental media related to groundwater in China (2009–2019), J. Hazard. Mater. 399 (2020), 122813.

[4] X. Yu, J. Huang, J. Zhao, S. Liu, D. Xiang, Y. Tang, J. Li, Q. Guo, X. Ma, J. Zhao, Efficient visible light photocatalytic antibiotic elimination performance induced by nanostructured Ag/AgCl@Ti^{3+}–TiO$_2$ mesocrystals, Chem. Eng. J. 403 (2021), 126359.

[5] C. Zhang, G. Zeng, D. Huang, C. Lai, M. Chen, M. Cheng, W. Tang, L. Tang, H. Dong, B. Huang, X. Tan, R. Wang, Biochar for environmental management: Mitigating greenhouse gas emissions, contaminant treatment, and potential negative impacts, Chem. Eng. J. 373 (2019) 902–922.

[6] S. Xiao, D. Zhang, D. Pan, W. Zhu, P. Liu, Y. Cai, G. Li, H. Li, A chloroplast structured photocatalyst enabled by microwave synthesis, Nat. Commun. 10 (2019) 1570.

[7] H. Luo, Z. Zeng, G. Zeng, C. Zhang, R. Xiao, D. Huang, C. Lai, M. Cheng, W. Wang, W. Xiong, Y. Yang, L. Qin, C. Zhou, H. Wang, Y. Zhou, S. Tian, Recent progress on metal-organic frameworks based- and derived-photocatalysts for water splitting, Chem. Eng. J. 383 (2020), 123196.

[8] D. Qin, Y. Zhou, W. Wang, C. Zhang, G. Zeng, D. Huang, L. Wang, H. Wang, Y. Yang, L. Lei, S. Chen, D. He, Recent advances in two-dimensional nanomaterials for photocatalytic reduction of CO$_2$: insights into performance, theories and perspective, J. Mater. Chem. A 8 (2020) 19156–19195.

[9] Y. Yang, C. Zhou, W. Wang, W. Xiong, G. Zeng, D. Huang, C. Zhang, B. Song, W. Xue, X. Li, Z. Wang, D. He, H. Luo, Z. Ouyang, Recent advances in application of transition metal phosphides for photocatalytic hydrogen production, Chem. Eng. J. 405 (2021), 126547.

[10] Q. Zhang, L. Jiang, J. Wang, Y. Zhu, Y. Pu, W. Dai, Photocatalytic degradation of tetracycline antibiotics using three-dimensional network structure perylene diimide supramolecular organic photocatalyst under visible-light irradiation, Appl. Catal. B Environ. 277 (2020), 119122.

[11] S. Dong, L. Cui, W. Zhang, L. Xia, S. Zhou, C.K. Russell, M. Fan, J. Feng, J. Sun, Double-shelled ZnSnO$_3$ hollow cubes for efficient photocatalytic degradation of antibiotic wastewater, Chem. Eng. J. 384 (2020), 123279.

[12] Y. Yang, X. Li, C. Zhou, W. Xiong, G. Zeng, D. Huang, C. Zhang, W. Wang, B. Song, X. Tang, X. Li, H. Guo, Recent advances in application of graphitic carbon nitride-based catalysts for degrading organic contaminants in water through advanced oxidation processes beyond photocatalysis: a critical review, Water Res. 184 (2020), 116200.

[13] Z. Wang, H. Wang, Z. Zeng, G. Zeng, P. Xu, R. Xiao, D. Huang, X. Chen, L. He, C. Zhou, Metal-organic frameworks derived Bi$_2$O$_2$CO$_3$/porous carbon nitride: a nanosized Z-scheme systems with enhanced photocatalytic activity, Appl. Catal. B Environ. 267 (2020), 118700.

[14] W. Wang, C. Zhou, Y. Yang, G. Zeng, C. Zhang, Y. Zhou, J. Yang, D. Huang, H. Wang, W. Xiong, X. Li, Y. Fu, Z. Wang, Q. He, M. Jia, H. Luo, Carbon nitride based photocatalysts for solar photocatalytic disinfection, can we go further? Chem. Eng. J. 404 (2021), 126540.

[15] D. He, C. Zhang, G. Zeng, Y. Yang, D. Huang, L. Wang, H. Wang, A multifunctional platform by controlling of carbon nitride in the core-shell structure: from design to construction, and catalysis applications, Appl. Catal. B Environ. 258 (2019), 117957.

[16] J. Ran, W. Guo, H. Wang, B. Zhu, J. Yu, S.Z. Qiao, Metal-free 2D/2D phosphorene/ g-C$_3$N$_4$ Van der Waals heterojunction for highly enhanced visible-light photocatalytic H$_2$ production, Adv. Mater. 30 (2018) 1800128.

[17] C. Li, Q. Cao, F. Wang, Y. Xiao, Y. Li, J.J. Delaunay, H. Zhu, Engineering graphene and TMDs based van der Waals heterostructures for photovoltaic and photoelectrochemical solar energy conversion, Chem. Soc. Rev. 47 (2018) 4981–5037.

[18] Y. Qin, H. Li, J. Lu, Y. Feng, F. Meng, C. Ma, Y. Yan, M. Meng, Synergy between van der waals heterojunction and vacancy in ZnIn$_2$S$_4$/g-C$_3$N$_4$ 2D/2D photocatalysts for enhanced photocatalytic hydrogen evolution, Appl. Catal. B Environ. 277 (2020), 119254.

[19] H. Dong, S. Hong, P. Zhang, S. Yu, Y. Wang, S. Yuan, H. Li, J. Sun, G. Chen, C. Li, Metal-free Z-scheme 2D/2D VdW heterojunction for high-efficiency and durable photocatalytic H$_2$ production, Chem. Eng. J. 395 (2020) 125150.

[20] H. Song, Y. Wang, Z. Li, M. Huang, J. Yu, Y. Wu, Atomically thin two-dimensional ZnSe/ZnSe(ea)x van der Waals nanojunctions for synergistically enhanced visible light photocatalytic H$_2$ evolution, Nanoscale 11 (2019) 17718–17724.

[21] T. Li, W. Luo, H. Kitadai, X. Wang, X. Ling, Probing the domain architecture in 2D α-Mo$_2$C via polarized Raman spectroscopy, Adv. Mater. 31 (2019), 1807160.

[22] Y. Zhou, W. Wang, C. Zhang, D. Huang, C. Lai, M. Cheng, L. Qin, Y. Yang, C. Zhou, B. Li, H. Luo, D. He, Sustainable hydrogen production by molybdenum carbide-based efficient photocatalysts: from properties to mechanism, Adv. Colloid Interface Sci. 279 (2020), 102144.

[23] Q. Liang, H. Jin, Z. Wang, Y. Xiong, S. Yuan, X. Zeng, D. He, S. Mu, Metal-organic frameworks derived reverse-encapsulation Co-NC@Mo$_2$C complex for efficient overall water splitting, Nano Energy 57 (2019) 746–752.

[24] H. Kim, B. Anasori, Y. Gogotsi, H.N. Alshareef, Thermoelectric properties of two-dimensional molybdenum-based MXenes, Chem. Mater. 29 (2017) 6472–6479.

[25] H. Lin, N. Liu, Z. Shi, Y. Guo, Y. Tang, Q. Gao, Cobalt-doping in molybdenum-carbide nanowires toward efficient electrocatalytic hydrogen evolution, Adv. Funct. Mater. 26 (2016) 5590–5598.

[26] J. Dong, Y. Shi, C. Huang, Q. Wu, T. Zeng, W. Yao, A New and stable Mo-Mo$_2$C modified g-C$_3$N$_4$ photocatalyst for efficient visible light photocatalytic H$_2$ production, Appl. Catal. B Environ. 243 (2019) 27–35.

[27] J. Zhang, M. Wu, B. He, R. Wang, H. Wang, Y. Gong, Facile synthesis of rod-like g-C$_3$N$_4$ by decorating Mo$_2$C co-catalyst for enhanced visible-light photocatalytic activity, Appl. Surf. Sci. 470 (2019) 565–572.

[28] H. Cheng, T. Kamegawa, K. Mori, H. Yamashita, Surfactant-free nonaqueous synthesis of plasmonic molybdenum oxide nanosheets with enhanced catalytic activity for hydrogen generation from ammonia borane under visible light, Angew. Chem. Int. Ed. 53 (2014) 2910–2914.

[29] J. Wan, J. Wu, X. Gao, T. Li, Z. Hu, H. Yu, L. Huang, Structure confined porous Mo$_2$C for efficient hydrogen evolution, Adv. Funct. Mater. 27 (2017), 1703933.

[30] Q. Liang, X. Liu, J. Wang, Y. Liu, Z. Liu, L. Tang, B. Shao, W. Zhang, S. Gong, M. Cheng, Q. He, C. Feng, In-situ self-assembly construction of hollow tubular g-C$_3$N$_4$ isotype heterojunction for enhanced visible-light photocatalysis: Experiments and theories, J. Hazard. Mater. 401 (2021), 123355.

[31] C. Zhang, Y. Zhou, W. Wang, Y. Yang, C. Zhou, L. Wang, L. Lei, D. He, H. Luo, D. Huang, Formation of Mo$_2$C/hollow tubular g-C$_3$N$_4$ hybrids with favorable charge transfer channels for excellent visible-light-photocatalytic performance, Appl. Surf. Sci. 527 (2020), 146757.

[32] W. Wang, Q. Niu, G. Zeng, C. Zhang, D. Huang, B. Shao, C. Zhou, Y. Yang, Y. Liu, H. Guo, W. Xiong, L. Lei, S. Liu, H. Yi, S. Chen, X. Tang, 1D porous tubular g-C$_3$N$_4$ capture black phosphorus quantum dots as 1D/0D metal-free photocatalysts for oxytetracycline hydrochloride degradation and hexavalent chromium reduction, Appl. Catal. B Environ. 273 (2020), 119051.

[33] Y. Orooji, M. Ghanbari, O. Amiri, M. Salavati-Niasari, Facile fabrication of silver iodide/graphitic carbon nitride nanocomposites by notable photo-catalytic performance through sunlight and antimicrobial activity, J. Hazard. Mater. 389 (2020), 122079.

[34] J. Gong, Y. Li, Y. Zhao, X. Wu, J. Wang, G. Zhang, Metal-free polymeric (SCN)n photocatalyst with adjustable bandgap for efficient organic pollutants degradation and Cr(VI) reduction under visible-light irradiation, Chem. Eng. J. 402 (2020), 126147.

[35] Y. Yang, G. Zeng, D. Huang, C. Zhang, D. He, C. Zhou, W. Wang, W. Xiong, B. Song, H. Yi, S. Ye, X. Ren, In situ grown single-atom cobalt on polymeric carbon nitride with bidentate ligand for efficient photocatalytic degradation of refractory antibiotics, Small 16 (2020), 2001634.

[36] H. Yan, Y. Xie, Y. Jiao, A. Wu, C. Tian, X. Zhang, L. Wang, H. Fu, Holey reduced graphene oxide coupled with an Mo$_2$N-Mo$_2$C heterojunction for efficient hydrogen evolution, Adv. Mater. 30 (2018).

[37] Z.-h Yang, J. Cao, Y.-p Chen, X. Li, W.-p Xiong, Y.-y Zhou, C.-y Zhou, R. Xu, Y.-r Zhang, Mn-doped zirconium metal-organic framework as an effective adsorbent for removal of tetracycline and Cr(VI) from aqueous solution, Micro Mesopor. Mat. 277 (2019) 277–285.

[38] C. Zhang, W. Wang, A. Duan, G. Zeng, D. Huang, C. Lai, X. Tan, M. Cheng, R. Wang, C. Zhou, W. Xiong, Y. Yang, Adsorption behavior of engineered carbons and carbon nanomaterials for metal endocrine disruptors: experiments and theoretical calculation, Chemosphere 222 (2019) 184–194.

[39] Z. Wu, Y. Liang, X. Yuan, D. Zou, J. Fang, L. Jiang, J. zhang, H. Yang, Z. Xiao, MXene Ti$_3$C$_2$ derived Z-scheme photocatalyst of graphene layers anchored TiO$_2$/ g-C$_3$N$_4$ for visible light photocatalytic degradation of refractory organic pollutants, Chem. Eng. J. 394 (2020) 124921.

[40] W. Xu, S. Lai, S.C. Pillai, W. Chu, Y. Hu, X. Jiang, M. Fu, X. Wu, F. Li, H. Wang, Visible light photocatalytic degradation of tetracycline with porous Ag/graphite carbon nitride plasmonic composite: Degradation pathways and mechanism, J. Colloid Interface Sci. 574 (2020) 110–121.

[41] T. Pan, D. Chen, W. Xu, J. Fang, S. Wu, Z. Liu, K. Wu, Z. Fang, Anionic polyacrylamide-assisted construction of thin 2D–2D WO$_3$/g-C$_3$N$_4$ step-scheme heterojunction for enhanced tetracycline degradation under visible light irradiation, J. Hazard. Mater. 393 (2020) 122366.

[42] H. Dong, X. Zhang, J. Li, P. Zhou, S. Yu, N. Song, C. Liu, G. Che, C. Li, Construction of morphology-controlled nonmetal 2D/3D homojunction towards enhancing photocatalytic activity and mechanism insight, Appl. Catal. B Environ. 263 (2020), 118270.

[43] S. He, C. Yan, X.-Z. Chen, Z. Wang, T. Ouyang, M.-L. Guo, Z.-Q. Liu, Construction of core-shell heterojunction regulating α-Fe$_2$O$_3$ layer on CeO$_2$ nanotube arrays enables highly efficient Z-scheme photoelectrocatalysis, Appl. Catal. B Environ. 276 (2020), 119138.

[44] Y.-Y. Chen, Y.-L. Ma, J. Yang, L.-Q. Wang, J.-M. Lv, C.-J. Ren, Aqueous tetracycline degradation by H$_2$O$_2$ alone: Removal and transformation pathway, Chem. Eng. J. 307 (2017) 15–23.

[45] M. Yan, Y. Wu, F. Zhu, Y. Hua, W. Shi, The fabrication of a novel Ag$_3$VO$_4$/WO$_3$ heterojunction with enhanced visible light efficiency in the photocatalytic degradation of TC, Phys. Chem. Chem. Phys. 18 (2016) 3308–3315.

[46] Y. Xu, Y. Lin, X. Liu, Y. Luo, H. Xue, B. Huang, Q. Chen, Q. Qian, Electrospun BiOCl/Bi$_2$Ti$_2$O$_7$ nanorod heterostructures with enhanced solar light efficiency in the photocatalytic degradation of tetracycline hydrochloride, ChemCatChem 10 (2018) 2496–2504.

[47] Q. Gao, X. Zhao, Y. Xiao, D. Zhao, M. Cao, A mild route to mesoporous Mo$_2$C–C hybrid nanospheres for high performance lithium-ion batteries, Nanoscale 6 (2014) 6151–6157.

[48] M. Nowak, B. Kauch, P. Szperlich, Determination of energy band gap of nanocrystalline SbSI using diffuse reflectance spectroscopy, Rev. Sci. Instrum. 80 (2009), 046107.

[49] X. Yue, S. Yi, R. Wang, Z. Zhang, S. Qiu, Well-controlled SrTiO$_3$@Mo$_2$C core-shell nanofiber photocatalyst: boosted photo-generated charge carriers transportation and enhanced catalytic performance for water reduction, Nano Energy 47 (2018) 463–473.

[50] Y. Zou, D. Ma, D. Sun, S. Mao, C. He, Z. Wang, X. Ji, J.-W. Shi, Carbon nanosheet facilitated charge separation and transfer between molybdenum carbide and graphitic carbon nitride toward efficient photocatalytic H$_2$ production, Appl. Surf. Sci. 473 (2019) 91–101.

[51] X. Yue, S. Yi, R. Wang, Z. Zhang, S. Qiu, A novel architecture of dandelion-like Mo$_2$C/TiO$_2$ heterojunction photocatalysts towards high-performance photocatalytic hydrogen production from water splitting, J. Mater. Chem. A 5 (2017) 10591–10598.